JOURNAL OF INFORMATION SCIENCE AND ENGINEERING 39, 1155-1168 (2023)
DOI: 10.6688/JISE.202309_39(5).0009

# Volume Manipulations for Assisting Joint Surgery Diagnoses and Simulations

MING-SHIUM HSIEH[1,2], HIDEO YOKOTA[3] AND MING-DAR TSAI[4,+]
[1]*Department of Orthopedics Surgery*
*En Chu Kong Hospital*
*New Taipei, 237 Taiwan*
[2]*Department of Orthopedics*
*Taipei Medical University Hospital*
*Taipei, 110 Taiwan*
[3]*Center for Advanced Photonics, RIKEN, Japan*
[4]*Department of Information and Computer Engineering*
*Chung Yuan Christian University*
*Chungli, 320 Taiwan*
[+]*E-mail: mingdar@cycu.edu.tw*

Volume visualization has widely used to assist medical diagnoses but still not to provide accurate joint pathology diagnoses, because CT or MR slices are usually not taken at the critical position inducing joint morphological pathology. This study proposes a volume manipulation method that segments and reconstructs anatomic structures of a joint and uploads their surface vertices to GPU, respectively. The vertices recorded in GPU are used to multiply with the same matrix for structure reposition, and different matrices for structure deformation manipulations. Real-time visual responses are achieved because time-consuming surface reconstruction and reloading the vertices to GPU are not required. Experimental results shows the surgeons can reposition related structures of a joint to their respective critical positions for accurate diagnoses about the joint morphology pathology, and simulate surgical procedures to confirm if the planned surgery can correct the pathology through the proposed system based on the developed method.

***Keywords:*** volume visualization, volume manipulation, human computer interaction, computer assisted surgery diagnosis, surgery simulation

## 1. INTRODUCTION

Anatomical structure surfaces reconstructed from a volume constituted by parallel CT or MR slices have assisted diagnoses and surgery planning [1]. After the initial surface reconstruction, 3D images of any perspective for the structure surfaces can be processed by the standard graphics pipeline to achieve quick visual responses [2]. The volume visualization tools have widely applied such as equipped in CT or MR imaging machines or as free third-party software in PCs. However, current volume visualization methods cannot provide 3D images to assist accurate joint pathology diagnoses and further surgery planning, because the CT or MR slices are usually taken at a supine position not the critical position [3, 4]. At the latter, some related joint structures begin to induce morphological pathology, while they did usually not induce the pathology at the supine position.

As the examples used in the study, knee or shoulder joints provide a good degree of

Received June 5, 2022; revised August 31, 2022; accepted October 1, 2022.
Communicated by Chun-Rong Huang.
[+] Corresponding author.

activity for the lower extremity. The former supports the body weight and the latter mainly for output force. At these joints, morphology pathology by bone spurs or fractures, or torn soft tissues easily occurs to limit relative motions between the joint structures and bring degenerative arthritis. The high prevalence of knee and shoulder symptoms result in that the knee and shoulder surgeries occupy the highest proportion among all joint surgeries. For accurate diagnosis and surgical planning of a joint surgery, every structure (bone or soft tissue) of this joint should be repositioned from the supine to its respective critical position that may be not the same as the ones of other structures. To achieve the above purpose, every joint structure should be segmented, reconstructed and uploaded the surface vertices to GPU, respectively. CT slices cannot provide clear soft tissue boundaries so that are seldom used for joint surgery unless MR scanning machines are not available. Meanwhile, automatic segmentations are still difficult to be achieved for 3D MR slices [5]. For the reposition, rotation axes and centers of joint structures are required [6], but difficult to calculate without any specified marker [7]. For automatic diagnoses, some properties such distances between structures are also required.

This study proposes a volume manipulation method to achieve the purpose of accurate joint diagnoses and surgical planning. First, anatomic structures of a joint are segmented and their axes are determined by semi-automation that has to use the surgeons' specifications. The surface vertices of each segmented object are reconstructed and uploaded to GPU, respectively. A structure reposition is multiplying a transformation matrix to all the structure vertices, and a structure deformation is multiplying different transformation matrices to respective structure vertices. Because reconstruction or loading object vertices to GPU are not required again by the vertex shader program [8], quick visual responses for the transformations can be achieved. Through the proposed system based on the developed methods, surgeons can reposition related structures of a joint to their respective critical positions for accurate diagnose of the joint morphological pathology and simulate surgical procedures for confirming if the planned surgery can correct the pathology. Therefore, our contributions include the volume manipulation method for object reposition, deformation, feature (axis and distance) determination. The contribution also include the system that combines the proposed and our previous methods to assist joint pathology diagnoses, surgery planning and simulation rehearsal.

## 2. RELATED WORK

Volume data have been manipulated (changing voxel values and positions) to achieve various representations of volumetric objects. For example, shifting voxel position represented tissue deformations during surgical cut or incision [9, 10], and decreasing voxel density (gray-level) represented bone erosion by cutting [11]. However, change of one voxel (as $V_1$ shown in Fig. 1) position or value may bring changes of multiple surface vertices (as $P$ and $Q$). Therefore, multiple surface vertices cannot be represented by only one voxel value. Some methods extended a voxel with 6 distance-levels to represent possible vertices and thus their independent changes along $x$, $-x$, $y$, $-y$, $z$ and $-z$ axis direction from the voxel center until the neighboring voxel center [12], as $P$ between $V_1$ until $V_2$ in Fig. 1.

The distance-levels represented with the volume coordinates are then represented as vertices with the world coordinates to upload to GPU for rendering using the graphics pipe line. However, in cutting simulation, several vertices may change positions, or be added or deleted that must be reloaded to GPU to represent the surface change after cutting. If the vertices were uploaded in one-triangle units, uploading only the new triangles to and deleting old vertices in GPU are enabled to avoid reloading all the object vertices again to achieve real-time visual responses [13]. A distance-level; meanwhile, should also represent a surface change in a haptic (1000HZ) response. For example, a 256-level distance-level of 2.56mm-wide voxel can represent the surface change by 10mm/s tool feeding rate.

Together with the six distance-levels, six corresponding face-flags (as $F$ and $Fa$ corresponding to $P$ and $Q$, respectively, shown in Fig. 1) can represent topologic changes of an object at this voxel ($V$). All voxel faces of an object form a closed surface, thus can be used as boundaries to stop seed-flooding used for searching all voxels of the object [14]. By using various boundary and filling conditions, separation, removal, fusion and translation of anatomic structures (bones or prosthetic components) in spine surgery [15], ossicle surgery [16], hip surgery [17], and knee surgery [12] were simulated. The surface vertices of a new anatomic structure can be reconstructed and uploaded to GPU respectively to manipulate or to render by a specific color.

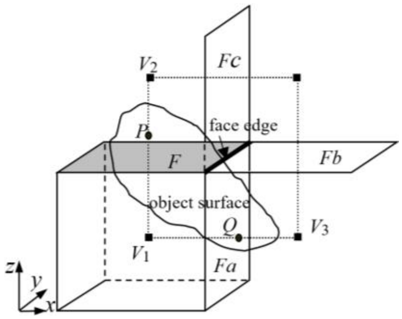


Fig. 1. Surface vertices from voxel distance-levels and topology represented by face-flags.

## 3. VOLUME MANIPULATION BY TRANSFORMING VERTICES OF RECONSTRUCTED SURFACES

This section explicitly details the method of manipulating a reconstructed object by transforming the object vertices. We apply every vertex ($\boldsymbol{V'}$) with a matrix ($\boldsymbol{Mv}$) that is a concatenation of a translation ($\boldsymbol{T}$), a rotation ($\boldsymbol{R}$) and scaling matrices ($\boldsymbol{S}$) to transform (reposition, resize, and suture) the object as shown in Eq. (1). Meanwhile, $\boldsymbol{N}$, the surface normal at the vertex is multiplied by $\boldsymbol{Mn}$, a concatenation of $\boldsymbol{R}$, and $\boldsymbol{S}$. $\boldsymbol{V'}$ and $\boldsymbol{N'}$ are the new position and associated surface normal for every vertex after the transformation.

$$\boldsymbol{V' = MvV = RTSV}, \qquad \boldsymbol{N' = MnN = RSN}. \tag{1}$$

Because the order of the object vertices and the topological relations among primitives (triangles) formed from the vertices are unchanged after the manipulation, changing or reloading any vertex to GPU is not required in the manipulation. It is a linear (affine) transformation (reposition or scaling) if the same concatenated transformation matrices

(***Mv*** and ***Mn***) are applied to all vertices and associated surface normals of the object. Otherwise, it is a deformation.

### 3.1 Affine Transformations of Reposition and Scaling

In an object reposition, scaling matrix is an identity. The same translation (***T***) and rotation (***R***) as shown in Fig. 2 are multiplied to every object vertex. ***T*** is determined by the translation vector $\vec{v}$, starting from the structure rotation center (***A***) to its expected position (***A′***) after the translation. ***R*** is calculated by the rotation center and axis with the rotation angle $\theta$, or determined by a point on the axis (***B***) and its expected position (***B′***). In a scaling, the transformation matrix is considered by concatenating from two matrices, ***Sw*** and ***Sv***. ***Sw*** represents scaling along the rotation axis ($\overleftrightarrow{\boldsymbol{A'B'}}$). Its ratio can be specified directly, or set as $(|\overline{\boldsymbol{AB}}|/|\overline{\boldsymbol{A'B'}}|)$. ***Sv*** represents scaling along the direction perpendicular to the rotation axis. Its ratio relates the one of ***Sw***, as the inverse of the square root to keep the volume of the manipulated structure conserved. The content of this section has been presented in a conference held in Honolulu, Hi, USA, on July 17-21, 2018 [18].

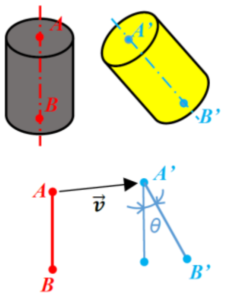


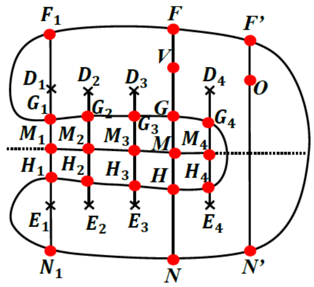


Fig. 2. Affine transformation of volumetric object. Fig. 3. Local deformation of volumetric object.

### 3.2 Local Deformation of Suturing

In an object deformation such as tissue suturing, variable scaling matrices (***S*** in Eq. 1) are applied to respective vertices of the torn tissue. These matrices are determined by pairs of points (as $\boldsymbol{D_1}$ and $\boldsymbol{E_1}$, $\boldsymbol{D_2}$ and $\boldsymbol{E_2}$, and $\boldsymbol{D_3}$ and $\boldsymbol{E_3}$ shown in Fig. 3) where the needle entered and exited the tissue for suturing. First, a line connecting every pair of entered and exited points (as $\boldsymbol{D_1}$ and $\boldsymbol{E_1}$) is used to obtain four intersections with the boundary voxel faces of the broken tissue (as $\boldsymbol{F_1}$, $\boldsymbol{G_1}$, $\boldsymbol{H_1}$, and $\boldsymbol{N_1}$). The inside two intersections (as $\boldsymbol{G_1}$ and $\boldsymbol{H_1}$) are considered as on the wound boundary and determine a midpoint (as $\boldsymbol{M_1}$). Two neighboring midpoints (as $\boldsymbol{M_1}$ and $\boldsymbol{M_2}$) determine a middle plane which passes the line connecting the two midpoints and is perpendicular to this line. The wound along this line is sutured if the tissue surfaces were extended from the wound boundary to the middle of the wound (as $|\overline{\boldsymbol{F_1G_1}}|$ or $|\overline{\boldsymbol{H_1N_1}}|$ extended to $|\overline{\boldsymbol{F_1M_1}}|$ or $|\overline{\boldsymbol{M_1N_1}}|$ using the scaling matrix with the ratio of $|\overline{\boldsymbol{F_1M_1}}|/|\overline{\boldsymbol{F_1G_1}}|$ or $|\overline{\boldsymbol{M_1N_1}}|/|\overline{\boldsymbol{H_1N_1}}|$). The surface vertices of the tissue on the line connecting a pair of entered and exited points multiplying the scaling matrix.

After the middle plane calculation, every tissue vertex (as ***V***) recorded in GPU is used to calculate the distance vectors from the vertex to all the middle planes and choose the shortest one (as $\overleftrightarrow{\boldsymbol{VM}}$) among these distances. ***M*** is the intersection with the middle plane with the shortest distance. When four intersections (as $\boldsymbol{F}$, $\boldsymbol{G}$, $\boldsymbol{H}$, and $\boldsymbol{N}$) are obtained from the intersection of the shortest distance vector ($\overleftrightarrow{\boldsymbol{VM}}$) with the boundary voxel face, the inside two intersections ($\boldsymbol{G}$ and $\boldsymbol{H}$) are used to determine the scaling matrix with the scaling ratio ($\overline{\boldsymbol{FM}}/\overline{\boldsymbol{FG}}$) for repositioning the vertex. When only two intersections ($\boldsymbol{F'}$ and $\boldsymbol{N'}$) are obtained from the shortest distance vector, no tear thus this structure vertex (as $\boldsymbol{O}$) is not repositioned. The torn part of the tissue is sutured after processing all tissue vertices.

## 4. VOLUME MANIPULATIONS FOR JOINT SURGERY PLANNING

This section describes the computer system for assisting joint surgery diagnoses and surgery planning and the calculation for object (joint structure) axes and thickness, and distance between structures.

### 4.1 3D Interface for Specifying Object Boundaries and Axes and Manipulations

Fig. 4 shows the proposed computer system and the interface through which a surgeon can ***segment*** a structure (bone or soft tissue) by using 6D inputs (position $\boldsymbol{H}$ and axis $\boldsymbol{Z}$) of a haptic device to specify borders (as blue curves in the right part of the interface) surrounding each 3D joint structure in an input CT or MRI volume [19]. Each border is specified on a CT or MRI cross-sectional slice that can be an original transversal, sagittal or coronal slice or one resliced from the original slices. The original slice number is usually small because of limitation by the compulsory health insurance in Taiwan, thus the slices are interpolated for accurate bordering and structure manipulations, and for fine voxel width to obtain high-quality visual and haptic responses during the volume manipulations.

The segmented structures are stored in **volume data**, so that the **surface reconstruction** module of the system can use the data to reconstruct surface vertices of the structure and uploads them to GPU for visual responses. Through the **volume manipulation** module, the surgeon can reposition (translate or rotate) a joint structure such as the shoulder humerus shown in the left-top part of the interface. Before the reposition, the surgeon may assign a (red) quadrilateral passing the structure to determine the rotating axis and center of the structure (details described in the following subsection). A yellow tool simulated by the 6D haptic inputs shown in the left-bottom part of the interface and can be used to specify structure reposition, simulate bone separation [12] and shaping [13]. These volume manipulations may give visual responses through the **surface reconstruction** module, or give haptic responses through the **3D haptic rendering** module.

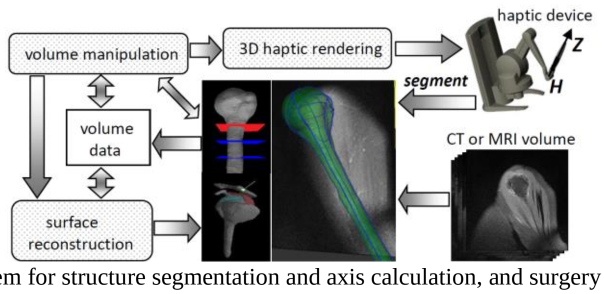


Fig. 4. System for structure segmentation and axis calculation, and surgery simulations.

### 4.2 Volume Manipulation for Calculating Rotation Axis of Structure

To determine the structure axis, three (as, *I*, *J* and *K* shown in Fig. 5 (a)) of the four vertices of a (red) quadrilateral are specified. For shoulder or knee surgery, the plane should be specified near to the surgical neck of the humerus or femur, and perpendicular to the humerus or femur shaft. Successive (2~4) planes parallel to the specified plane (as the blue planes) are automatically assigned. From each plane, the intersection of a closed loop with the structure is calculated to determine a closed loop (as *L*1 shown in Fig. 5 (b)). The intersection may also generate inside loops (as *L*2) that ae not used in determining the axis. The average of the loop faces (as *P* on *L*1 shown in Figs. 5 (b) and (c)) is the loop center that is considered near the axis. Therefore, centers of the closed loops from the specified and assigned plans are used to regress the axis. The rotational center on the axis can be the intersection with the axis by the specified plane or specified by another plane.

All the boundary faces on a closed loop connect one by one, thus can be searched out from a beginning boundary face (as *P* in Fig. 5 (b)). For example, a boundary face (*F* in Fig. 1) with the surface normal parallel to *z* axis has *x*, –*x*, *y* and –*y* edges. Therefore, there are three sharing faces for an edge (as *Fa*, *Fb* and *Fc* for the *x*-edge (bold line shown in Fig.1). Totally, there are 12 edge-sharing faces for a processed (specified or assigned) face on the loop. Each of the 12 edge-sharing faces is check if it is boundary. The distances from the edge-sharing boundary faces to the processed plane are calculated to choose the one with the shortest distance (as *Fy* is chosen as the next face of *Fz* in Fig. 5 (d)). The same procedure is repeated until the searched next face is the beginning face.

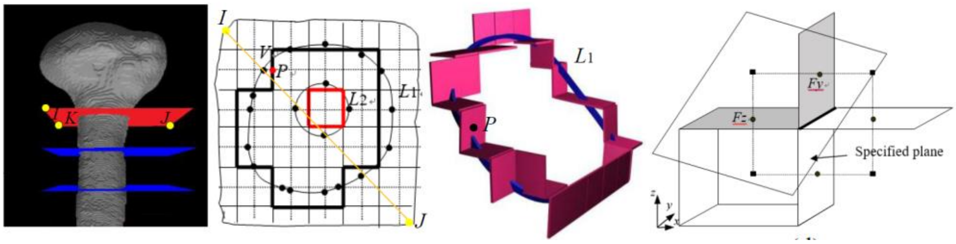


Fig. 5. Structure axis determination; (a) Specified and assigned planes; (b) Cross-sectional intersection (closed loops) of a plane with the structure; (c) Outmost loop represented by voxel faces; (d) Determination of next boundary face on the loop.

The beginning boundary face is searched out by a 3D DDA algorithm [20], which traverses the processed plane voxel by voxel along either diagonal line (as from the vertices *I* to *J* of the quadrilateral shown in Figs. 5 (a) and (b)). At a traversed voxel, the distances from the boundary faces of this voxel to the processed plane are calculated to find the face with the smallest distance. If this distance is under half voxel length, it is set as the beginning face (as *P* shown in Fig. 5 (b)), otherwise the voxel traversal continues.

### 4.3 Calculation of Distance Between Structures

The distance between two objects as bones in a joint is important for diagnosis and surgery planning in joint surgery. Because soft tissue (as muscle, bursa, *etc.*) usually locates between two bones, too short distance indicates the in-between tissue will be wounded to bring degenerative arthritis to cartilage on the bones and tear at the soft tissue. The distance is calculated as the one between two parallel planes tangent to a bone and its opposite rotating bone.

All vertices of an object uploaded to GPU are compared to find out the vertex (as *P* in Fig. 6) with the minimum or maximum coordinate (*e.g.*, the inferior along the gravity direction) and to calculate the tangent plane by the vertices and their associated surface normals. To determine the plane parallel to the tangent and passing the opposite object, vertices and their associated surface normals of the opposite object uploaded to GPU are used to calculate the distances from the vertices to the tangent plane along their surface normals, and thus to find out the vertex (as *Q*) with the shortest distance to the tangent plane. For a repositioned object or opposite object, the reposition matrix is applied to their vertices and associated surface normals prior to the distance calculation.

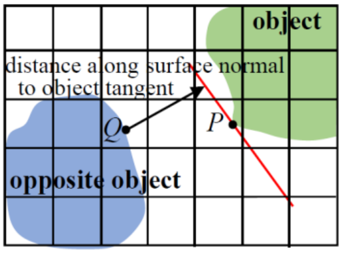


Fig. 6. Distance calculation for an object and its opposite object.

## 5. EXPERIMENTAL RESULTS AND DISCUSSION

A surgeon (the first author) used the prototype system to diagnose joint morphological pathology, plan surgical procedures and confirm if the pathological morphology can be corrected by the planned procedures for to knee and shoulder joint surgery. In the following, one example with shoulder impingement syndrome and one example with broken knee cruciate ligament and torn meniscus are demonstrated. Currently, the system has been implemented on a PC with Intel i7-4790k CPU, NVIDIA Quadro K2200 graphics card, and PHANToM Desktop haptic device (Geomagic Inc.). GPU-base OpenGL is used for graphics pipeline programming [8].

### 5.1 Shoulder Surgery and Simulation by Volume Manipulation

Subacromial impingement syndrome (SAIS) caused by narrow acromiohumeral distance (AHD) accounts for the commonest (44%-65%) disorder of the shoulder. AHD is defined as the shortest distance between the acromial inferior and the humeral head [21]. The failure rate of acromioplasty (standard surgery for SAIS) is high (10%-30%) [22]. A major reason is considered as sufficient AHD was not achieved to release the impingement at the soft tissue still pinged in-between the acromion and humerus, or the remaining acromion was insufficient to keep shoulder stability [23]. The proposed manipulation volume method calculated the acromial thickness for removal to decompress SAIS and keep should shoulder stability. Fig. 7 shows an example of a female patient with informed consent obtained to demonstrate diagnoses and surgery planning by the system.

Fig. 7 (a) shows the 3D image from a 91-slices volume interpolated from 16 sagittal MR slices taken at a supine posture. The surgeon took about 1h to segment bones (grey) of humerus and scapula, a muscle (red), and cartilage (light blue) on the humerus. He then specified a (red) plane to recognize the acromion (highlighted as blue as shown in Fig. 7 (b)) from the scapula as a separate structure by a volume manipulation [14]. Surface vertices of the structure are reconstructed and loaded to GPU, and can be rendered as another color. The acromial inferior (Fig. 7 (b)) was recognized by comparing the coordinates of all vertices of the acromion. The AHD (3.2mm as $d$ in Fig. 7 (c)) were calculated by the distance calculation method between a tangent (red) plane at the acromial inferior and its parallel (red) plane passing the humeral head cartilage. The acromial thickness from the inferior spur was calculated as 10.7 mm ($a$ in Fig. 7 (c)) by comparing the coordinates of the acromion vertices. Because the original acromial thickness without the spur was estimated as 8 mm ($b$ in Fig. 7 (c), an average mean thickness [24]), the spur is calculated as 2.7mm. The surgeon then specified a (red) plane to recognize the humerus shaft (highlighted as blue in Fig. 7 (d)) and calculate the shaft axis. The rotation center was specified by another plane passing the shaft axis to intersect the center in Fig. 7 (e). The arm (humerus) was then repositioned (rotated) outward to the impingement degree based on the patient's pain complaints, there the scapula including the acromion was repositioned (translated) to let the acromion and humerus touch the opposite sides of the soft tissue with torn position in Fig. 7 (f). In this position, the AHD was calculated as 1.8mm. The AHD was too small both at the impingement and supine positions to confirm the diagnosis of a SAIS.

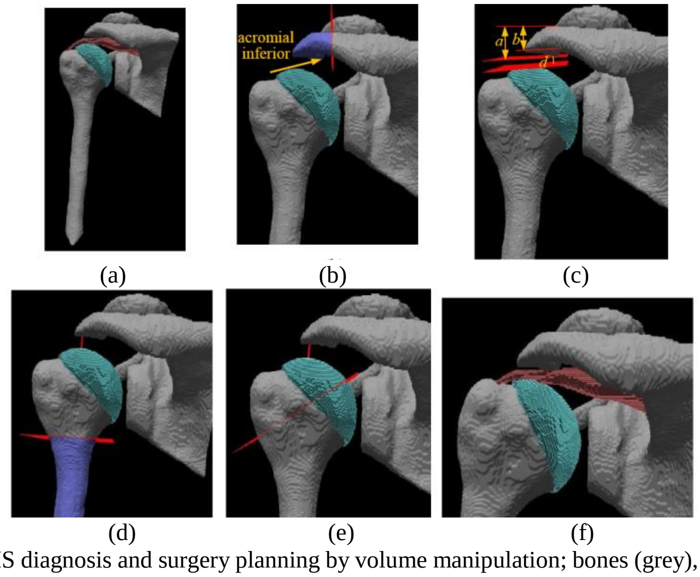


Fig. 7. A SAIS diagnosis and surgery planning by volume manipulation; bones (grey), muscle (red), and cartilage (light blue); all posterior views; (a) 3D image at supine position; (b) Recognition of acronomin and acromial inferior calcualtion; (c) Calcuations of acromion thickness and AHD; (d) and (e) Determination of humerus shaft axis and rotation center; (f) Reposition to impingement and AHD calculation at this position.

Because the contraction rate is considered as linear [24], the target AHD can be calculated by the AHD at the supine and the impingement positions. It was calculated as 8.3 mm at the supine position for releasing the impingement even the arm was elevated horizontally. The target acromial thickness for removal was calculated as over 5.1 (8.3 – 3.2) mm for solving the SAIS. Besides, the remaining thickness should be over half (4mm) of the original acromial thickness [25], thus acromial thickness for removal should be under 6.7 (10.7 – 4) mm to avoid the shoulder instability. Based on the calculated removal acromial thickness together with the shoulder morphology (3D images), the surgeon can plan the procedures to remove acromial thickness between 5.1~6.7 mm.

Fig. 8 shows the surgeon used the simulation functions of the system to confirm and rehearse the surgical procedures for improving the successful rate of acromioplasty. First, the humerus was pulled (repositioned) outward to enlarge the space between the humerus and scapula for bone shaping as in real surgery in Fig. 8 (a). Fig. 8 (b) shows the efficient bone shaping using a large bur (yellow) was first used. Fig. 8 (c) shows fine (polishing) bone-shaping using a small bur in which the humerus was repositioned back to reveal the enlarged subacromial space by the bone shaping. Fig. 8 (d) shows the torn muscle, and Fig. 8 (e) shows the sutured muscle after suturing simulation. Fig. 8 (f) shows the SAIS was solved because the acromial inferior was removed, the subacromial space was enlarged with the muscle not impinged ay the original impingement position, and the remaining acromial thickness was sufficient to keep the joint stability. The prognosis result showed the shoulder can move without pains in daily life after planned surgery.

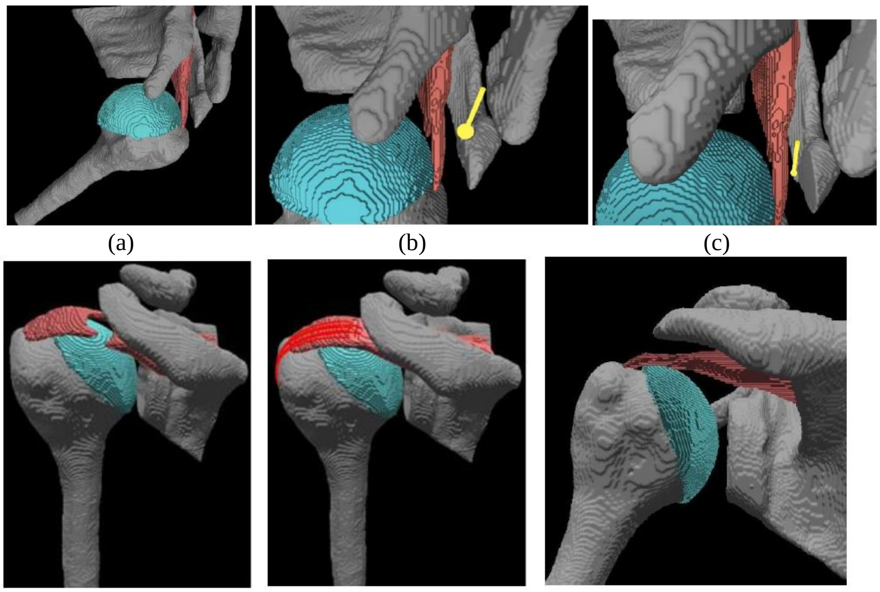

(a) (b) (c)
(d) (e) (f)

Fig. 8. Acromioplasty simulations for shoulder SAIS surgery planning by volume manipulation; bones (grey), muscle (red), and cartilage (light blue); bones (grey), muscle (red), and cartilage (light blue); burs in bone-shaping (yellow); (a)-(c) Oblique view; (d)-(f) Posterior views; (a) Repositioned humerus to enlarge the space at the acromion; (b) Efficeint bone shaping with a large bur; (c) Fine bone shaping with a small bur; (d) Torn and; (e) Sutured muscle; (f) Enlarged subacromial space at the original impingement position after surgery.

### 5.2 Knee Surgery and Simulation by Volume Manipulation

Fig. 9 shows the 3D images obtained from a set of 96-slice volume interpolated from 20 transversal MR slices of a male with informed consent was obtained for this study who suffered a knee pain caused by a falling down. A typical meniscal tear associated with cruciate ligament injury was doubted [26]. This example shows the diagnoses and surgery planning using the proposed methods and system. Fig. 9 (a) shows the surgeon segmented bones (grey) of fumes, tibia and patella, several muscles and ligaments (green). The surgeon confirmed a nearly broken anterior cruciate ligament (ACL) by the 3D images of various perspectives. The surgeon chose an optimal ligament graft from a set of templates. The graft was sliced with the same resolution as the volume and reconstructed to obtain the surface vertices and shown together with the knee structures (Fig. 9 (a)). The surgeon used the scaling function to change graft dimension, and the reposition function to insert the graft into the original position of ACL for confirming the graft dimension and morphology in Fig. 9 (b). In the insertion, the patella (kneecap bone) together with surrounding tendons were repositioned away to reveal the ACL reconstruction as real surgery.

In diagnose and surgical planning of the meniscal tear, the surgeon rotated the femur to observe the hidden meniscus. He specified a (red) plane as shown in Fig. 9 (c) passing between the femur neck to recognize the femur shaft (blue) and calculate the shaft axis and rotation center. The surgeon then used the axis and center to reposition away the femur, then observe and diagnose a torn medial meniscus as shown in Fig. 9 (d). Fig. 9 (e) shows the surgeon was suturing the torn meniscus based on the planned procedures. Fig. 9 (f) shows the sutured tear provided comfortable morphology for the repaired meniscus. The prognosis results show the knee can move without pain in daily life after surgery.

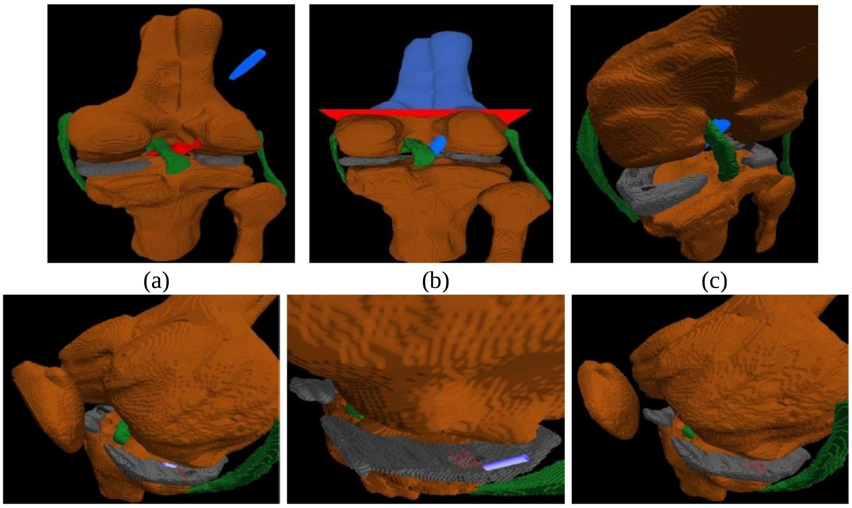

(a) (b) (c)

(d) (e) (f)

Fig. 9. Diagnosis and surgery planning for knee meniscal tear associated with cruciate ligament injury by volume manipulation; Bones (earth yellow), meniscus (gray), ligament (green); (a)-(b) Posterior views; (c) Oblique views, (d)-(f) Lateral vie; (a) Nearly broken ACL (red) and candidate graft ligament (blue); (b) Reconstructed ACL and femurol shaft (blue); (c) Femur reposition for diagnos-ing torn meniscus; (d) Meniscus in suturing, suture lines (red), suture needle (blue); (e) Zoom-in image for the suturing; (f) Sutured meniscus.

### 5.3 Method Evaluation and Comparison

The proposed volume manipulation method used a transformation matrix to multiply all vertices of an object for the object reposition. A visual response includes the time for multiplying the same matrix to all vertices of the repositioning object and for rendering all objects in the volume, both proportional to the object vertex numbers. Table 1 shows some response results from the knee and shoulder surgery examples. The total vertices numbers are about 760,000 for the shoulder and 1180, 000 for the knee example, respectively. The vertex numbers of the repositioning structures, and response time are shown in Table 1.

Meanwhile, a straightway of object reposition (only translation) swaps voxel contents of an object to the translated new position. The visual response increases apparently for large objects, because it requires seed-flooding to traverse all voxels of the object for swapping. The visual response of this method also includes surface reconstruction for the object vertices at the new position and delete the vertices reconstructed at the old position. It totally takes over 5 minutes and much more than our method (1 second) for the same scapula example.

**Table 1. Visual responses for repositioning objects.**

| reposition structure | scapula (shoulder) | muscle (shoulder) | femur (knee) | graft (knee) |
|---|---|---|---|---|
| visual response (sec.) | 1.0 | 0.8 | 1.6 | 1.2 |
| repositioned vertices (no.) | 420,000 | 33,000 | 570,000 | 2,700 |

## 6. CONCLUSIONS

In this paper, we proposed a volume manipulation method to represent volumetric object reposition, scaling and local deformation by multiplying surface vertices of respective objects, and calculate object axes and distances between objects by traversing object voxels. Experimental results show the system based on the developed methods combining with our reported manipulation method can assist the accurate diagnoses and surgery planning for joint surgery, and used for the surgery rehearsal to improve successful surgery rate.

## ACKNOLEDEGEMENT

We sincerely thank colleagues in the departments of radiology and orthopedic surgery of En Chu Kong Hospital for their efforts in the assistance during the system development, pre-operative diagnoses and post-operative prognoses. This study was supported by the Ministry of Science and Technology, Taiwan/ROC (Grant No. MOST-104-2221-E-033-035-My2).

## REFERENCES

1. W. E. Lorensen and H. E. Cline, “Marching cubes: A high resolution 3D surface construction algorithm,” in *Proceedings of ACM SIGGraph Computer Graphics*, 1987, pp. 163-169.

2. Y. L. Moon, K. Sugamoto, A. Paoluzzi, A. D. Carlo, J. Kwak, D. S. Shin, D. O. Kim, D. H. Lee, and J. Kim, "Standardizing in 3D medical imaging," *Computer*, Vol. 47, 2014, pp. 76-79.
3. Y. D. Song, N. P. Jain, S. J. Kim, S. K. Kwon, M. J. Chang, C. B. Chang, and T. K. Kim, "Is knee magnetic resonance imaging over-utilized in current practice," *Knee Surgery & Related Research*, Vol. 27, 2015, pp. 95-100.
4. A. Lorenzetti, J. J. Streit, A. F. Cabezas, K. N. Christmas, J. LaMartina, P. Simon, and M. A. Frankle, "Bone graft augmentation for severe glenoid bone loss in primary reverse total shoulder arthroplasty: outcomes and evaluation of host bone contact by 2D-3D image registration," *JBJS Open Access*, Vol. 2, 2017, e0015.
5. H. Lee, H. Hong, and J. Kim, "Segmentation of anterior cruciate ligament in knee MR images using graph cuts with patient-specific shape constraints and label refinement," *Computers in Biology and Medicine*, Vol. 55, 2014, pp. 1-10.
6. C. Amabile, A. M. J. Bull, and A. E. Kedgley, "The centre of rotation of the shoulder complex and the effect of normalisation," *Journal of Biomechanics*, Vol. 49, 2016, pp. 1938-1943.
7. C. Charbonnier, S. Chagué, F. C. Kolo, J. C. K. Chow, and A. Lädermann, "A patient-specific measurement technique to model shoulder joint kinematics," *Orthopaedics and Traumatology: Surgery and Research*, Vol. 100, 2014, pp.715-719.
8. E. Angel and D. Shreiner, *Interactive Computer Graphics: A Top-Down Approach with Shader-Based OpenGL*, Addison Wesley, Boston, 2011.
9. P. A. Heng, C. Y. Cheng, T. T. Wong, and T. S. Xu, "A virtual-reality training system for knee arthroscopic surgery," *IEEE Transactions on Information Technology in Biomedicine*, Vol. 8, 2004, pp. 217-227.
10. I. Berndt, R. Torchelsen, and A. Maciel, "Efficient surgical cutting with position-based dynamics," *IEEE Computer Graphics and Applications*, Vol. 37, 2017, 24-31.
11. D. Morris, C. Sewell, F. Barbagli, N. H. Blevins, and S. Girod, "Visuohaptic simulation of bone surgery for training and evaluation," *IEEE Computer Graphics and Applications*, Vol. 26, 2006, pp. 48-57.
12. M. D. Tsai and M. S. Hsieh, "Volume manipulations for simulating bone and joint surgery," *IEEE Transactions on Information Technology in Biomedicine*, Vol. 9, 2005, pp. 139-149.
13. M. D. Tsai and M. S. Hsieh, "Accurate visual and haptic burring surgery simulation based on a volumetric model," *Journal of X-ray Science and Technology*, Vol.18, 2010, pp. 1-17.
14. S. B. Jou and M. D. Tsai, "A fast seed filling algorithm," *The Visual Computer*, Vol.19, 2003, pp. 243-251.
15. M. D. Tsai and M. S. Hsieh, "A spine surgery simulator based on volumetric models," *Biomedical Engineering: Applications Basis and Communications*, Vol. 27, 2015, Article ID 1550005.
16. M. S. Hsieh, F. P. Lee, and M. D. Tsai, "A virtual reality ear ossicle surgery simulator using three-dimensional computer tomography," *Journal of Medical and Biological Engineering*, Vol. 30, 2010, pp. 53-63.
17. M. S. Hsieh, M. D. Tsai, and Y. D. Yeh, "Three-dimensional hip morphology analysis using CT transverse sections to automate diagnoses and surgery managements," *Computers in Biology and Medicine*, Vol. 35, 2005, pp. 347-371.

18. M. D. Tsai, M. S. Hsieh, and H. Yokota, "Volume manipulation based on 3D reconstructed surfaces for joint function evaluation and surgery simulation," in *Proceedings of the 40th Annual International Conference of the IEEE Engineering in Medicine & Biology Society*, 2018, pp. 969- 972.
19. T. Ijiri, S. Yoshizawa, Y. Sato, M. Ito and H. Yokota, "Bilateral Hermite radial basis functions for contour-based volume segmentation," *Computer Graphics Forum*, Vol. 32, 2013, pp. 123-132.
20. D. Cohen-Or and A. Kaufman, "3D line voxelization and connectivity control," *IEEE Computer Graphics and Applications*, Vol. 17, 1997, pp. 80-87.
21. D. Goutallier, P. Leguilloux, J. M. Postel, C. Radier, J. Bernageaud and S. Zilber, "Acromio humeral distance less than six millimeter: Its meaning in full-thickness rotator cuff tear," *Orthopaedics & Traumatology: Surgery & Research*, Vol. 97, 2011, pp. 246-251.
22. A. Bouchard, J. Garret, L. Favard, H. Charles, and D. Ollat, "Failed subacromial decompression, risk factors," *Orthopedics & Traumatology: Surgery & Research*, Vol. 100S, 2014, pp. S365-S369.
23. A. Pillai, V. Eranki, J. Malal, and G. Nimon, "Outcomes of open subacromial decompression after failed arthroscopic acromioplasty," *ISRN Surgery*, 2012, Article ID 806843.
24. L. J. Hébert, H. Moffet, M. Dufour, and C. Moisan, "Acromiohumeral distance in a seated position in persons with impingement syndrome," *Journal of Magnetic Resonance Imaging*, Vol. 18, 2003, pp. 72-79.
25. R. S. Thakkar, S. C. Thakkar, U. Srikumarn, E. G. McFarland, and L. M. Fayad, "Complications of rotator cuff surgery – the role of post-operative imaging in patient care," *The British Journal of Radiology*, Vol. 87, 2014, Article ID 20130630.
26. T. Hagino, S. Ochiai, S. Senga, T. Yamashita, M. Wako, T. Ando, and H. Haro, "Meniscal tears associated with anterior cruciate ligament injury," *Archives of Orthopaedic and Trauma Surgery*, Vol. 135, 2015, pp. 1701-1706.

**Ming-Shium Hsieh (謝銘勳)** received an MD degree from Taipei Medical University, Taiwan, and Ph.D. degree in Orthopedic Surgery from Essen University, Germany. He is on the faculty of the Department of Orthopedics at Taipei Medical University, and also En Chu Kong Hospital, Taiwan. His research interests include image studies, computer application in medicine, and orthopedics including spinal surgery, arthroplasty, traumatology, and basic research of orthopedics.

**Hideo Yokota (横田秀夫)** received the BS and MS degrees in Agriculture and Veterinary Medicine, Department of Zoology, Nihon University, and Ph.D. degree in Precision Machinery Engineering from the University of Tokyo, Japan. He is the leader of Image Processing Research Team, RIKEN Center for Advanced Photonics. His research interests include computer graphics, image processing, and scientific visualization and computer applications in medicine and biology.

**Ming-Dar Tsai (蔡明達)** received a BS degree in Mechanical Engineering from National Taiwan University, Taiwan, and MS and Ph.D. degrees in Precision Machinery Engineering from the University of Tokyo, Japan. He is a member of the faculty of the Department of Information and Computer Engineering of Chung Yuan Christian University, Taiwan. His research interests include computer graphics, image processing, and scientific visualization and computer applications in medicine and biology.